ChemPubSoc Europe

DOI: 10.1002/open.201800051

Open Access ChemistryOPEN Full Papers

Intrinsic Dynamic Nature of Neutral Hydrogen Bonds Elucidated with QTAIM Dual Functional Analysis: Role of the Compliance Force Constants and QTAIM-DFA Parameters in Stability

Taro Nishide, Satoko Hayashi,* and Waro Nakanishi*[a]

The dynamic and static nature of various neutral hydrogen bonds (nHBs) is elucidated with quantum theory of atoms-in-molecules dual functional analysis (QTAIM-DFA). The perturbed structures generated by using the coordinates derived from the compliance force constants (C_{ij}) of internal vibrations are employed for QTAIM-DFA. The method is called CIV. The dynamic nature of CIV is described as the "intrinsic dynamic nature", as the coordinates are invariant to the choice of the coordinate system. nHBs are, for example, predicted to be van der Waals (H_2Se—*—HSeH; *=bond critical point), *t*-HB_{nc} (*typical*-HBs with no covalency: HI—*—HI), *t*-HB_{wc} (*t*-HBs with covalency: H_2C=O—*—HI), CT-MC [molecular complex formation through charge transfer (CT): H_2C=O—*—HF], and CT-TBP (trigonal bipyramidal adduct formation through CT: H_3N—*—HI) in nature. The results with CIV were the same as those with POM in the calculation errors, for which the perturbed structures were generated by partial optimization, and the interaction distances in question were fixed suitably in POM. The highly excellent applicability of CIV for QTAIM-DFA was demonstrated for the various nHBs, as well as for the standard interactions previously reported. The stability of the HBs, evaluated by ΔE, is well correlated with C_{ij} ($\Delta E \times C_{ij}$=constant value of −165.64), and the QTAIM parameters, although a few deviations were detected.

1. Introduction

Hydrogen bonds (HBs) are fundamentally important because of their ability to form molecular associations, which stabilizes a system in terms of energy; the direction of the interacting three atoms in B···H–Y (see below) is controlled through the formation of a HB that is almost a linear asymmetric σ bond (3c–4e: three-center, four-electron bond).[1–6] Weak HBs can be considered to be van der Waals (vdW) interactions, whereas strong HBs tend to be more covalent (Cov) in nature. The formation of HBs plays a crucial role in all fields of chemical and biological sciences. HBs control various chemical processes depending on their strength. It is imperative to clarify the nature of HBs for better understanding of chemical processes controlled by HBs.[7–10] We previously reported the dynamic and static nature of HBs in the neutral and charged forms by applying the quantum theory of atoms-in-molecules dual functional analysis (QTAIM-DFA).[11–16] Perturbed structures were employed for QTAIM-DFA to clarify the dynamic behavior of the interactions. The perturbed structures were generated by using the normal coordinates of the (best-fitted) internal vibrations and/or by partial optimization, for which the interaction distances in question were suitably fixed. The methods are called NIV[14–16] and POM,[11–13] respectively. Neutral HBs (nHBs) are predicted to be vdW to CT-TBP [trigonal bipyramidal adduct formation through charge transfer (CT)] in nature, whereas charged HBs are typically Cov in nature.[17]

B-*-HY (**1**–**29**) [B···H—Y]

B = H_2Se, H_2S, H_2O, H_2CO, H_3N, and HX (X = I, Br, Cl, and F)
Y= SeH, SH, OH, NH_2, I, Br, Cl, and I

The QTAIM approach, introduced by Bader,[18,19] enables us to analyze the nature of chemical bonds and interactions.[20–31] Many QTAIM investigations have been reported, mainly by theoretical researchers, and experimental scientists have recently used QTAIM to explain their results by considering chemical bonding and interactions.[20–39] A bond critical point (BCP, *)[40] is an important concept in QTAIM, for which $\rho(\boldsymbol{r})$ (charge density) reaches a minimum along the interatomic (bond) path, whereas it is a maximum on the interatomic surface separating the atomic basins. The $\rho(\boldsymbol{r})$ at the BCP is described by $\rho_b(\boldsymbol{r}_c)$ and so are other QTAIM functions, such as the total electron

[a] *T. Nishide, Dr. S. Hayashi, Prof. W. Nakanishi*
Wakayama University
Faculty of Systems Engineering
Wakayama (Japan)
E-mail: hayashi3@sys.wakayama-u.ac.jp
nakanisi@sys.wakayama-u.ac.jp

Supporting Information and the ORCID identification number(s) for the author(s) of this article can be found under: https://doi.org/10.1002/open.201800051.

energy densities $H_b(\boldsymbol{r}_c)$, potential energy densities $V_b(\boldsymbol{r}_c)$, and kinetic energy densities $G_b(\boldsymbol{r}_c)$ at the BCPs. A chemical bond or interaction between A and B is denoted by A–B, which corresponds to a bond path (BP) in QTAIM. We will use A–*–B for a BP, in which the asterisk emphasizes the existence of a BCP in A–B.[18,19,40] Equations (1), (2), and (2′) represent the relations between $G_b(\boldsymbol{r}_c)$, $V_b(\boldsymbol{r}_c)$, $H_b(\boldsymbol{r}_c)$, and $\nabla^2\rho_b(\boldsymbol{r}_c)$; $H_b(\boldsymbol{r}_c)$ must be negative if $\nabla^2\rho_b(\boldsymbol{r}_c) < 0$, as confirmed by Equation (2) with negative $V_b(\boldsymbol{r}_c)$ at all BCPs.

$$H_b(\boldsymbol{r}_c) = G_b(\boldsymbol{r}_c) + V_b(\boldsymbol{r}_c) \quad (1)$$

$$\left(\frac{\hbar^2}{8m}\right)\nabla^2\rho_b(\boldsymbol{r}_c) = H_b(\boldsymbol{r}_c) - \frac{V_b(\boldsymbol{r}_c)}{2} \quad (2)$$

$$= G_b(\boldsymbol{r}_c) + \frac{V_b(\boldsymbol{r}_c)}{2} \quad (2')$$

QTAIM-DFA was recently formulated on the basis of QTAIM.[41–48] The $H_b(\boldsymbol{r}_c)$ parameters are plotted versus $H_b(\boldsymbol{r}_c)-V_b(\boldsymbol{r}_c)/2$ $[=(\hbar^2/8m)\nabla^2\rho_b(\boldsymbol{r}_c)]$ at the BCPs in QTAIM-DFA. In our treatment, data from the perturbed structures around the fully optimized structures are employed, in addition to those from the fully optimized ones. Data from the fully optimized structures are analyzed by using the polar coordinate (R, θ) representation, which corresponds to the static natures of the interactions.[12–16] Each interaction plot, which contains data from both the perturbed structures and the fully optimized ones, includes a specific curve that provides important information about the interaction. This plot is expressed by (θ_p, κ_p), for which θ_p corresponds to the tangent line of the plot and κ_p is the curvature. The dynamic nature of the interactions has been proposed on the basis of (θ_p, κ_p).[12–16] Namely, the signs of the first and second derivatives of $H_b(\boldsymbol{r}_c)$ and $H_b(\boldsymbol{r}_c)-V_b(\boldsymbol{r}_c)/2$ $[=(\hbar^2/8m)\nabla^2\rho_b(\boldsymbol{r}_c)]$ are also employed to characterize the interactions in QTAIM-DFA, whereas the signs of $H_b(\boldsymbol{r}_c)$ and $H_b(\boldsymbol{r}_c)-V_b(\boldsymbol{r}_c)/2$ are employed for classification in QTAIM. We call (R, θ) and (θ_p, κ_p) the QTAIM-DFA parameters, which are drawn in Figure 2, exemplified by H_3N–*–HI (**26**: C_{3v}). QTAIM-DFA is applied to standard interactions, and rough criteria that distinguish the interaction in question from others are obtained. QTAIM-DFA and the criteria are explained in the Supporting Information by using Schemes S1 and S2, Figures S1, and Equations (S1)–(S7). The basic concept of the QTAIM approach is also discussed. QTAIM-DFA has excellent potential for evaluating, classifying, characterizing, and understanding weak to strong interactions according to a unified form.[12–16]

However, the predicted dynamic nature would somewhat change depending on the perturbed structures employed. Very recently, we proposed a new method to generate the perturbed structures, other than NIV and POM, for QTAIM-DFA.[49] The method employs the coordinates corresponding to the compliance force constants (C_{ij}) for the internal vibrations.[50–54] We call the method CIV.[49] The compliance force constants (C_{ij})[50–53,55] are defined as the partial second derivatives of the potential energy due to an external force, as shown in Equation (3), for which i and j refer to internal coordinates, and the force constants f_i and f_j correspond to i and j, respectively. The value in Equation (3) corresponds to a lower numerical value (i) of a compliance constant representing a stronger bond (j), that is, the compliance constants measure the flexibility (or compliance) of a particular bond. The applications of CIV to the closed-shell (CS) interactions are substantially more effective than those to the shared-shell (SS) interactions in QTAIM-DFA.[49]

$$C_{ij} = \frac{\partial^2 E}{\partial f_i \partial f_j} \quad (3)$$

The very high applicability of CIV is demonstrated to generate the perturbed structures for QTAIM-DFA. The dynamic nature of the interactions based on the perturbed structures with CIV is described as the "intrinsic dynamic nature of interactions", as the coordinates corresponding to C_{ij} are invariant to the choice of the coordinate system. The results with CIV are the same as those with POM in terms of the calculation errors. However, CIV has been applied only to the typical interactions of a limited number of HBs, and the default in NIV seems large for HBs.[49] The establishment of QTAIM-DFA on the firm basis of employing the perturbed structures with CIV for the wide range of nHBs is another purpose of this paper. The neutral HBs in the species examined in this work are denoted by B–*–HY (**1**–**29**), containing HI adducts, which are found in Table 1.

Herein, we present the results of investigations on the "intrinsic dynamic nature of nHBs", together with the static nature in B–*–HY (**1**–**29**). To elucidate the nature, QTAIM-DFA is applied to B–*–HY (**1**–**29**) by employing the perturbed structures generated with CIV. Each HB interaction in **1**–**29** is classified and characterized by employing the criteria obtained on the basis of the standard interactions as a reference. The applicability of CIV to QTAIM-DFA is also established in the nHBs of **1**–**29**, for which the QTAIM-DFA parameters elucidated by using CIV are compared with those elucidated by using NIV and POM. As a result, a firm basis for QTAIM-DFA by employing the perturbed structures generated with CIV is established over the wide range of the nHBs in **1**–**29**. The stability of **1**–**29** is discussed by examining the relations between the stability and the C_{ij}, (R, θ), and (θ_p, κ_p) values.

Computational Details

The 6-311++G(3df,3pd) basis sets of the Gaussian 09 programs[56] were employed for the calculations of **1**–**29**, together with the basis set of the 7433111/743111/7411/2+1s1p1d1f type for I, as implemented in the Sapporo Basis Set Factory.[57] The basis set system is called BSS-A. All calculations were performed under nonrelativistic conditions. The Møller–Plesset second-order energy correlation (MP2) level[58–60] was applied to the calculations (MP2/BSS-A). The optimized structures were confirmed by frequency analysis. To obtain the perturbed structures with POM, the optimized structures were further (partially) optimized by employing Z matrices. The distances in question in the perturbed structures (r) were fixed to satisfy Equation (4), in which r_o is the distance in the fully optimized structure with a_o of Bohr radius (0.52918 Å). The method to generate the perturbed structures with NIV is explained by Equa-

Table 1. QTAIM functions and QTAIM-DFA parameters evaluated for the neutral hydrogen bonds (nHBs) in **1**–**29** by applying the QTAIM dual functional analysis by employing the perturbed structures generated with CIV, NIV, and POM.[a,b]

Species (X–*–Y)	$c\nabla^2\rho_b(r_c)$[c] [au]	$H_b(r_c)$ [au]	$k_b(r_c)$[d]	R [au]	θ [°]	C_{ij}[e] [mDyn^{-1} Å^3]	$\theta_{p:CIV}$ [°]	$\kappa_{p:CIV}$ [au^{-1}]
H_2Se–*–HSeH (**1**)	0.0026	0.0006	−0.858	0.0027	*76.0*[f]	23.4	88.1	194
H_2S–*–HSH (**2**)	0.0032	0.0008	−0.861	0.0033	76.3	19.2	91.8	229
H_3N–*–HNH_2 (**3**)	0.0059	0.0016	−0.844	0.0062	74.9	12.1	87.5	188
H_2O–*–HOH (**4**)	0.0106	0.0005	−0.976	0.0107	87.3	6.4	123.7	159
H_3N–*–HOH (**5**)	0.0094	−0.0020	−1.096	0.0096	*102.1*[f]	5.5	157.3	87.3
HI–*–HI (**6**)	0.0034	0.0004	−0.945	0.0034	84.1	13.8	102.6	304
HBr–*–HBr (**7**)	0.0038	0.0010	−0.853	0.0039	75.6	17.9	91.4	269
HCl–*–HCl (**8**)	0.0049	0.0015	−0.828	0.0052	*73.6*	16.1	95.0	294
HF–*–HF (**9**)	0.0125	−0.0002	−1.007	0.0125	90.8	5.9	128.2	107
H_2Se–*–HI (**10**)	0.0040	0.0001	−0.986	0.0040	88.5	12.7	*126.5*[f]	464
H_2Se–*–HBr (**11**)	0.0040	0.0002	−0.978	0.0040	87.6	13.0	*130.1*[f]	488
H_2Se–*–HCl (**12**)	0.0044	0.0001	−0.989	0.0044	88.7	11.2	*137.3*[f]	431
H_2Se–*–HF (**13**)	0.0051	−0.0013	−1.113	0.0053	*104.3*[f]	7.3	164.5	146
H_2S–*–HI (**14**)	0.0043	0.0001	−0.991	0.0043	89.0	13.4	124.5	334
H_2S–*–HBr (**15**)	0.0047	−0.0001	−1.010	0.0047	91.1	12.0	133.9	309
H_2S–*–HCl (**16**)	0.0051	−0.0002	−1.024	0.0051	92.8	10.3	140.5	269
H_2S–*–HF (**17**)	0.0061	−0.0020	−1.143	0.0064	*108.5*[f]	6.6	165.1	120
H_2O–*–HI (**18**)	0.0091	0.0009	−0.949	0.0091	84.5	10.1	113.6	217
H_2O–*–HBr (**19**)	0.0103	−0.0006	−1.028	0.0103	93.2	8.2	138.6	182
H_2O–*–HCl (**20**)	0.0112	−0.0018	−1.072	0.0114	98.9	6.4	149.9	116
H_2O–*–HF (**21**)	0.0131	−0.0089	−1.252	0.0158	124.0	3.4	166.1	6.9
H_2C=O–*–HI (**22**)	0.0102	−0.0009	−1.044	0.0103	95.3	9.7	139.7	216
H_2C=O–*–HBr (**23**)	0.0108	−0.0022	−1.093	0.0111	*101.6*[f]	8.2	154.4	138
H_2C=O–*–HCl (**24**)	0.0115	−0.0032	−1.122	0.0119	*105.9*[f]	6.6	160.4	92.0
H_2C=O–*–HF (**25**)	0.0127	−0.0099	−1.279	0.0161	127.8	3.5	170.1	6.7
H_3N–*–HI (**26**)	0.0050	−0.0268	−1.728	0.0272	169.4	19.8	194.1	4.2
H_3N–*–HBr (**27**)	0.0069	−0.0189	−1.579	0.0201	160.0	7.9	190.3	6.4
H_3N–*–HCl (**28**)	0.0080	−0.0155	−1.492	0.0174	152.7	5.5	186.9	9.3
H_3N–*–HF (**29**)	0.0085	−0.0195	−1.533	0.0213	156.4	2.8	182.0	2.8

Species (X–*–Y)	$\theta_{p:POM}$ [°]	$\kappa_{p:POM}$ [au]	ν[g] [cm^{-1}]	k_f[h] [mDyn Å^{-1}]	$\theta_{p:NIV}$ [°]	$\kappa_{p:NIV}$ [au]	ΔE[i] [kJ mol^{-1}]	Predicted nature
H_2Se–*–HSeH (**1**)	88.0	202	41.8	0.016	88.3	196	−7.6	*p*-CS/vdW
H_2S–*–HSH (**2**)	91.8	232	69.1	0.009	93.3	263	−8.7	*p*-CS/*t*-HB_{nc}
H_3N–*–HNH_2 (**3**)	87.5	151	141.2	0.036	86.6	159	−13.8	*p*-CS/vdW
H_2O–*–HOH (**4**)	123.8	159	188.1	0.043	116.7	158	−22.2	*p*-CS/*t*-HB_{nc}
H_3N–*–HOH (**5**)	157.5	88.1	200.2	0.050	158.6	83.0	−28.2	*r*-CS/CT-MC
HI–*–HI (**6**)	102.7	309	43.5	0.024	102.5	296	−12.9	*p*-CS/*t*-HB_{nc}
HBr–*–HBr (**7**)	91.4	269	48.8	0.028	91.2	259	−8.3	*p*-CS/*t*-HB_{nc}
HCl–*–HCl (**8**)	95.0	295	76.4	0.021	94.8	267	−10.0	*p*-CS/*t*-HB_{nc}
HF–*–HF (**9**)	128.3	109	166.9	0.081	128.5	103	−20.7	*r*-CS/*t*-HB_{wc}
H_2Se–*–HI (**10**)	*126.5*[f]	464	52.5	0.031	*126.4*[f]	454	−14.5	*p*-CS/*t*-HB_{nc}
H_2Se–*–HBr (**11**)	130.0	498	57.9	0.044	*129.9*[f]	480	−13.9	*p*-CS/*t*-HB_{nc}
H_2Se–*–HCl (**12**)	137.4	438	79.3	0.057	137.1	423	−15.5	*p*-CS/*t*-HB_{nc}
H_2Se–*–HF (**13**)	164.5	151	123.0	0.101	163.9	144	−21.3	*r*-CS/CT-MC
H_2S–*–HI (**14**)	124.3	340	68.2	0.017	*125.3*[f]	325	−13.9	*p*-CS/*t*-HB_{nc}
H_2S–*–HBr (**15**)	133.9	317	77.5	0.028	134.3	301	−14.6	*r*-CS/*t*-HB_{wc}
H_2S–*–HCl (**16**)	140.6	274	98.2	0.042	140.7	260	−16.6	*r*-CS/*t*-HB_{wc}
H_2S–*–HF (**17**)	165.1	121	145.7	0.096	164.6	117	−23.2	*r*-CS/CT-MC
H_2O–*–HI (**18**)	112.9	212	97.6	0.013	122.9	227	−18.1	*p*-CS/*t*-HB_{nc}
H_2O–*–HBr (**19**)	138.1	186	119.6	0.034	140.7	168	−20.7	*r*-CS/*t*-HB_{wc}
H_2O–*–HCl (**20**)	149.9	120	150.1	0.048	*152.0*[j]	104	−24.7	*r*-CS/*t*-HB_{wc}[k]
H_2O–*–HF (**21**)	166.1	8.5	229.9	0.079	167.6	7.1	−38.4	*r*-CS/CT-MC
H_2C=O–*–HI (**22**)	139.8	202	141.9	0.049	138.3	219	−21.5	*r*-CS/*t*-HB_{wc}
H_2C=O–*–HBr (**23**)	154.5	135	152.0	0.070	152.8	140	−22.4	*r*-CS/CT-MC
H_2C=O–*–HCl (**24**)	160.4	91.7	176.0	0.115	158.6	91.8	−25.9	*r*-CS/CT-MC
H_2C=O–*–HF (**25**)	170.0	8.0	246.7	0.267	168.3	5.7	−36.3	*r*-CS/CT-MC
H_3N–*–HI (**26**)	194.2	5.3	100.7	0.025	193.9	4.2	−30.5	*r*-CS/CT-TBP
H_3N–*–HBr (**27**)	190.3	8.1	148.1	0.059	189.8	6.3	−33.7	*r*-CS/CT-TBP
H_3N–*–HCl (**28**)	186.9	11.7	186.8	0.105	186.2	9.3	−38.0	*r*-CS/CT-TBP
H_3N–*–HF (**29**)	181.9	5.4	227.0	0.241	180.6	1.8	−54.8	*r*-CS/CT-TBP

[a] The functions and parameters were evaluated at the BCPs of the nHBs in the fully optimized structures. [b] With MP2/6–311++G(3df,3pd), except for I, for which calculations were performed with (7433111/743111/7411/2+1s1p1d1f) from the Sapporo Basis Set Factory, which is called MP2/BSS-A. [c] $c\nabla^2\rho_b(r_c)=H_b(r_c)-V_b(r_c)/2$, for which $c=\hbar^2/8m$. [d] $k_b(r_c)=V_b(r_c)/G_b(r_c)$. [e] Defined in Equation (3). [f] Minor values that do not satisfy the characterization from the major ones are shown in italics. [g] Internal vibrational frequency corresponding to the interaction. [h] Force constant corresponding to the frequency. [i] From the components. [j] The nature of *r*-CS/CT-MC was predicted with NIV. [k] On the borderline area between *r*-CS/*t*-HB_{wc} and *r*-CS/CT-MC if evaluated with CIV and POM.

tion (5). A *k*-th perturbed structure in question ($\mathbf{S}_{kw}$) is generated by the addition of the normal coordinates of the *k*-th internal vibration ($\mathbf{N}_k$) to the standard orientation of a fully optimized structure ($\mathbf{S}_o$) in the matrix representation. The coefficient f_{kw} in Equation (5) controls the structural difference between $\mathbf{S}_{kw}$ and $\mathbf{S}_o$: f_{kw} is determined to satisfy Equation (4) for *r*. The selected motion must be most effectively localized on the interaction in question among the zero-point internal vibrations in NIV. Equations (4) and (6) are similarly applied to generate the perturbed structures with CIV, for which $\mathbf{C}_i$ is the coordinates corresponding to C_{ij} in Equation (3).[50–53,55] The $\mathbf{N}_k$ and $\mathbf{C}_i$ values of five digits are used to predict $\mathbf{S}_{kw}$ and $\mathbf{S}_{iw}$, respectively:

$$r = r_o + wa_o \quad [w = (0),\ \pm 0.05, \text{ and } \pm 0.1;\ a_o = 0.52918\ \text{Å}] \tag{4}$$

$$\mathbf{S}_{kw} = \mathbf{S}_o + f_{kw} \cdot \mathbf{N}_k \tag{5}$$

$$\mathbf{S}_{iw} = \mathbf{S}_o + f_{iw} \cdot \mathbf{C}_i \tag{6}$$

$$y = c_o + c_1 x + c_2 x^2 + c_3 x^3 \quad (R_c^2:\ \text{square of correlation coefficient}) \tag{7}$$

QTAIM functions are calculated by using the same basis sets at the MP2 level as in the optimizations (MP2/BSS-A), unless otherwise noted, and are analyzed with the AIM2000 program.[18,61] $H_b(\boldsymbol{r}_c)$ are plotted versus $H_b(\boldsymbol{r}_c)-V_b(\boldsymbol{r}_c)/2$ for the data of five data points of $w=0$, ± 0.05, and ± 0.1 in Equation (4) in QTAIM-DFA. Each plot is analyzed by using a regression curve of the cubic function, shown in Equation (7), for which $(x,\ y)=[H_b(\boldsymbol{r}_c)-V_b(\boldsymbol{r}_c)/2,\ H_b(\boldsymbol{r}_c)]$ ($R_c^2 >$ 0.99999 per usual).[16]

2. Results and Discussion

2.1. Optimized Structures of Neutral Hydrogen-Bonded Species and Stability

Neutral HB species, B–HY [**1**–**29**: B = H_2Se, H_2S, H_2O, H_2CO, H_3N, and HX (= HI, HBr, HCl, and HF); HY = HSeH, HSH, HOH, HNH_2, and HX], were optimized with MP2/BSS-A, although some were optimized in a previous study.[17] The optimized B–H distances [r_o(B, H)] are collected in Table S1, together with the sum of the vdW radii[62] [$\Delta r = r_o$(B, H)$-\Sigma r_{vdW}$(B, H)]. The symmetries are also given in Table S1. The energies for **1**–**29** on the energy surface (*E*) and the relative energies from the components (ΔE) [$= E$(HB)$-E$(components)] are collected in Table S1. The ΔE values of **1**–**29** are also shown in Table 1 for convenience of discussion. The ΔE values are plotted versus Δr for **1**–**29**. The plot is shown in Figure S2, and the correlation is given in the figure.[63]

The ΔE values of B–*–HX (B = H_2Se, H_2S, $H_2C{=}O$, and H_3N; HX = HF, HCl, HBr, and HI) are plotted versus those of H_2O–*–HX. The plot is shown in Figure S3, which also contains the plot of $\Delta E(H_2O$–*–HX) versus $\Delta E(H_2O$–*–HX) for convenience of comparison. The correlations are very good (Table 2, entries 1–4). The results show that the ΔE values of B–*–HX (B = H_2Se, H_2S, $H_2C{=}O$, H_2O, and H_3N) are well correlated with each other if the ΔE values of common HX are compared, although the ΔE value of H_2Se–*–HI seems somewhat smaller (more stable) than that predicted from the correlation for H_2Se–*–HX. The magnitudes of ΔE become larger in the order $H_2Se \leq H_2S \ll H_2O \leq H_2C{=}O \ll H_3N$, although $\Delta E(H_2O$–*–HF) $< \Delta E(H_2C{=}O$–*–HF). The relations between ΔE in B–*–HX are also confirmed in this work for HX = HI in addition to HX = HF, HCl, and HBr, although the *E* values are all evaluated under nonrelativistic conditions.

Table 2. Correlations in **1**–**29**, evaluated with NIV, POM, and CIV, under the MP2/BSS-A conditions.[a]

Entry	Correlation	*a*	*b*	R_c^2	*n*
1	ΔE_{H_2Se-HX} vs. ΔE_{H_2O-HX}	0.371	−6.83	0.960	4
2	ΔE_{H_2S-HX} vs. ΔE_{H_2O-HX}	0.468	−5.13	0.997	4
3	ΔE_{H_2CO-HX} vs. ΔE_{H_2O-HX}	0.751	−7.39	0.996	4
4	ΔE_{H_3N-HX} vs. ΔE_{H_2O-HX}	1.200	−8.72	0.9997	4
5	$\theta_{p:NIV}$ vs. $\theta_{p:CIV}$	0.988	1.71	0.994	29
6	$\theta_{p:NIV}$ vs. $\theta_{p:CIV}$	0.992	1.02	0.999	27[b]
7	$\theta_{p:POM}$ vs. $\theta_{p:CIV}$	1.001	−0.15	0.9999[7]	29
8	$\kappa_{p:NIV}$ vs. $\kappa_{p:CIV}$	0.980	−0.31	0.994	29
9	$\kappa_{p:POM}$ vs. $\kappa_{p:CIV}$	1.009	−0.42	0.998	29
10	ΔE vs. *R*	−2012.0	−3.83	0.866	27[c]
11	ΔE vs. θ	−0.479	25.70	0.891	27[c]
12	$\theta_{p:CIV}$ vs. θ	2.390	−86.95	0.957	23[d]
13	ΔE vs. $\theta_{p:CIV}$	−0.314	19.69	0.971	8[e]
14	ΔE vs. $\theta_{p:CIV}$	−0.219	14.01	0.957	8[f]
15	ΔE vs. $\theta_{p:CIV}$	−0.155	−0.05	0.838	6[g]
16	ΔE vs. $\theta_{p:CIV}$	1.994	−414.66	0.898	4[h]

[a] Analyzed by assuming the linear correlation $y = ax + b$ (R_c^2: square of correlation coefficient). [b] For **1**–**29**, except for **4** and **18**. [c] For **1**–**29**, except for **26** and **27**. [d] For **1**–**29**, except for **21**, **24**, and **25**–**29**. [e] For **1**–**9**, except for **3**. [f] For **10**–**17**. [g] For **18**–**25**, except for **21** and **25**. [h] For **24**–**29**.

After clarifying the basic behavior in Δr and ΔE, molecular graphs with contour plots of $\rho(\boldsymbol{r})$ are examined before detailed discussion of the nature of the nHBs in **1**–**29**.

2.2. Molecular Graphs with Contour Plots for B–*–HX

Figure 1 illustrates molecular graphs for B–*–HI (B = H_2Se, H_2S, H_2O, $H_2C{=}O$, H_3N, and HI) containing the contour plots of $\rho(\boldsymbol{r})$. All of the BCPs expected for B–*–HI are clearly detected. They seem to be well located at three-dimensional saddle points of $\rho(\boldsymbol{r})$. The molecular graphs of **1**–**29**, other than B–*–HI, were similarly drawn, and although they are not shown, they are very close to those of B–*–HI.

2.3. Survey of the B–*–HY Interactions

The HB interactions seem straight for B–*–HX on the basis of the BPs, as shown in Figure 1. To examine the linearity of the BPs, further, the lengths of the BPs (r_{BP}) in question are collected in Table S2 for **1**–**29**, together with the corresponding straight-line distances (R_{SL}). The differences between them ($\Delta r_{BP} = r_{BP} - R_{SL}$) are less than 0.04 Å. Consequently, the BPs for all B–*–HY of **1**–**29** can be described by straight lines.

QTAIM functions were calculated for B–*–HY (**1**–**29**) at the BCPs. Table 1 collects the $H_b(\boldsymbol{r}_c)-V_b(\boldsymbol{r}_c)/2$ [$=(\hbar^2/8m)\nabla^2\rho_b(\boldsymbol{r}_c)$] and $H_b(\boldsymbol{r}_c)$ values, and the $\rho_b(\boldsymbol{r}_c)$ values are given in Table S3, whereas some were reported previously.[17] The $H_b(\boldsymbol{r}_c)$ values

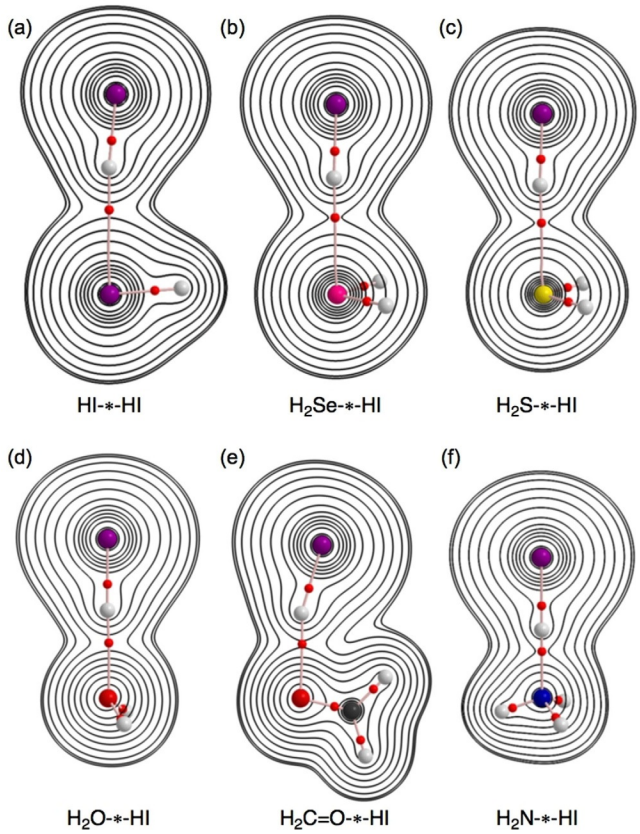

Figure 1. Molecular graphs, with contour plots of $\rho(r)$ for a) HI–*–HI (**6**), b) H_2Se–*–HI (**10**), c) H_2S–*–HI (**14**), d) H_2O–*–HI (**18**), e) H_2C=O–*–HI (**22**), and f) H_3N–*–HI (**26**).

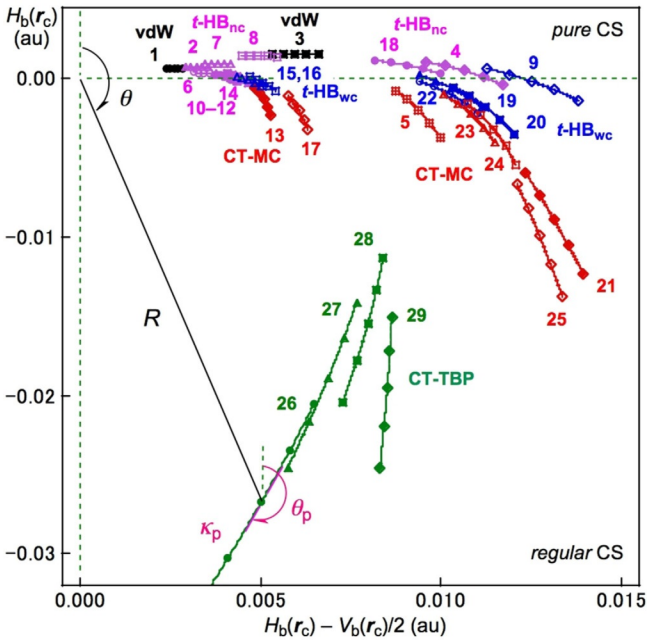

Figure 2. Plots of $H_b(r_c)$ versus $H_b(r_c)-V_b(r_c)/2$ for **1–29**, for which data from the perturbed structures generated with CIV were employed, in addition to the data from the optimized structures. Definitions of (R, θ) and (θ_p, κ_p) are illustrated, as exemplified by H_3N–*–HI (**26**: C_{3v}).

are plotted versus $H_b(r_c)-V_b(r_c)/2$ for the data shown in Table 1 together with those from the perturbed structures generated with CIV. Figure 2 shows the plots. The plots appear in the region of $H_b(r_c)-V_b(r_c)/2>0$; therefore, the HBs are all classified by CS interactions. The CS interactions will be further classified by the signs of $H_b(r_c)$. They are specifically called pure CS (p-CS) interactions if they appear in the region of $H_b(r_c)>0$, whereas they will be regular CS (r-CS) interactions for $H_b(r_c)<0$. The behavior of the nHBs in **1–29** will be discussed in detail after evaluations of the QTAIM-DFA parameters (see Table 1).

2.4. QTAIM-DFA Parameters of (R, θ) and (θ_p, κ_p) for Neutral HBs in 1–29 Evaluated with POM, NIV, and CIV

The QTAIM-DFA parameters of (R, θ) and (θ_p, κ_p) were obtained by analyzing the plots of $H_b(r_c)$ versus $H_b(r_c)-V_b(r_c)/2$ according to Equations (S3)–(S6). The (θ_p, κ_p) values evaluated by employing the perturbed structures generated with CIV, POM, and NIV are denoted by ($\theta_{p:CIV}$, $\kappa_{p:CIV}$), ($\theta_{p:POM}$, $\kappa_{p:POM}$), and ($\theta_{p:NIV}$, $\kappa_{p:NIV}$), respectively. The ($\theta_{p:CIV}$, $\kappa_{p:CIV}$) values can be obtained if the plots shown in Figure 2 are analyzed. Table 1 collects the QTAIM-DFA parameters for **1–29**. Table 1 contains the C_{ij} values for the nHBs in **1–29** together with the frequencies correlated to the NIVs employed to generate the perturbed structures and the force constants (k_f).

2.5. Behavior of $\theta_{p:CIV}$, $\theta_{p:POM}$, and $\theta_{p:NIV}$ Together with That of $\kappa_{p:CIV}$, $\kappa_{p:POM}$, and $\kappa_{p:NIV}$

Figure 3a shows the plot of $\theta_{p:NIV}$ versus $\theta_{p:CIV}$, which gives very good correlation. The correlation is shown in entry 5 of Table 2 (see also Figure 3a). The magnitudes of the differences between $\theta_{p:NIV}$ and $\theta_{p:CIV}$ ($\Delta\theta_{p:NIV-CIV}=\theta_{p:NIV}-\theta_{p:CIV}$) are less than 2° for most of the interactions. The magnitudes of $\Delta\theta_{p:NIV-CIV}$ are larger than 2.0° for H_2O–*–HOH ($\Delta\theta_{p:NIV-CIV}=-7.0°$),[49] H_2O–*–HI (9.3°), H_2O–*–HBr (2.1°), and H_2O–*–HCl (2.1°). Large deviations are detected for H_2O–*–HX (HX = HOH and HI). The selected internal vibration for H_2O–*–HX could not be located effectively on O–*–H by mixing with some other vibrational modes in the same symmetry,[49] although the selected mode is the best fit for the O–*–H interaction. The correlation for the plot is much improved (Table 2, entry 6; see also Figure 3a) if the data for H_2O–*–HX (X = HOH and HI) are omitted from the correlation. On the other hand, excellent correlation is obtained if $\theta_{p:POM}$ is plotted versus $\theta_{p:CIV}$, as shown in Figure 3b (for the correlation, also see Table 2, entry 7). The magnitudes of $\Delta\theta_{p:POM-CIV}$ are equal to or less than 0.1° for all HB adducts examined, except for H_3N–*–HOH ($\Delta\theta_{p:POM-CIV}=0.2°$), H_2S–*–HI (−0.2°), H_2O–*–HI (−0.7°), and H_2O–*–HBr (−0.5°). The results must be a reflection of the fact that the perturbed structures generated with POM and CIV are very similar.[49] The results demonstrate the excellent applicability of CIV to generate the perturbed structures also for the nHB species in QTAIM-DFA.

Figure 4a,b shows the plots of $\kappa_{p:NIV}$ versus $\kappa_{p:CIV}$ and $\kappa_{p:POM}$ versus $\kappa_{p:CIV}$. The correlations are given in entries 8 and 9 of Table 2 (see also Figure 4a,b, respectively). The correlations seem very good, although substantial deviations are observed

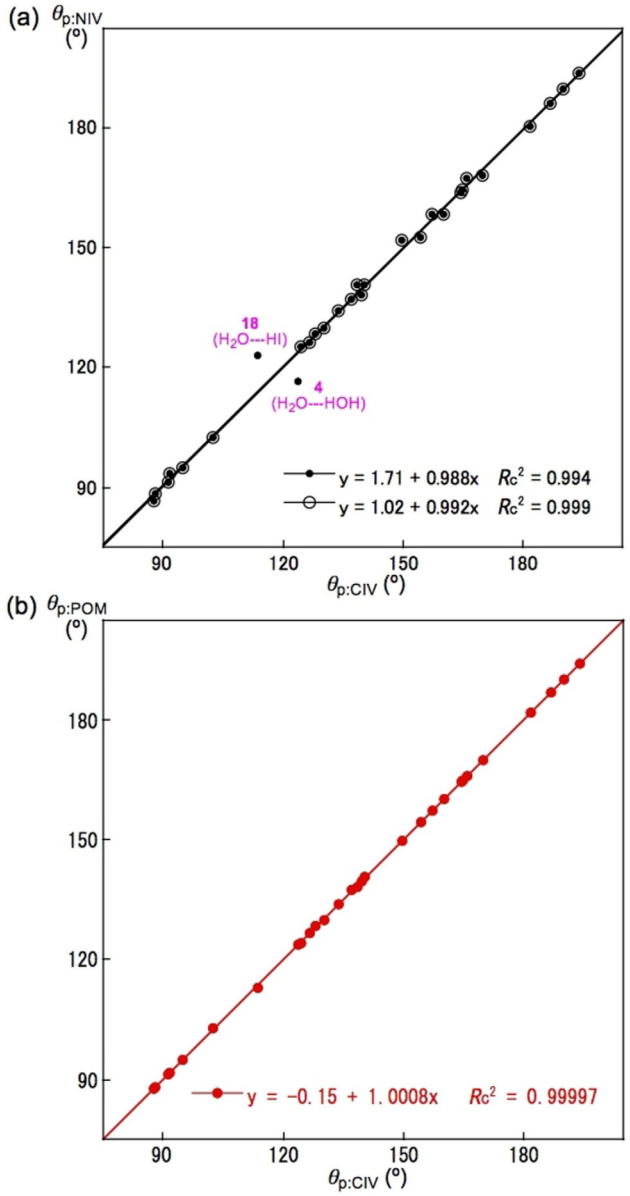

Figure 3. Plots of a) $\theta_{p:NIV}$ versus $\theta_{p:CIV}$ and b) $\theta_{p:POM}$ versus $\theta_{p:CIV}$.

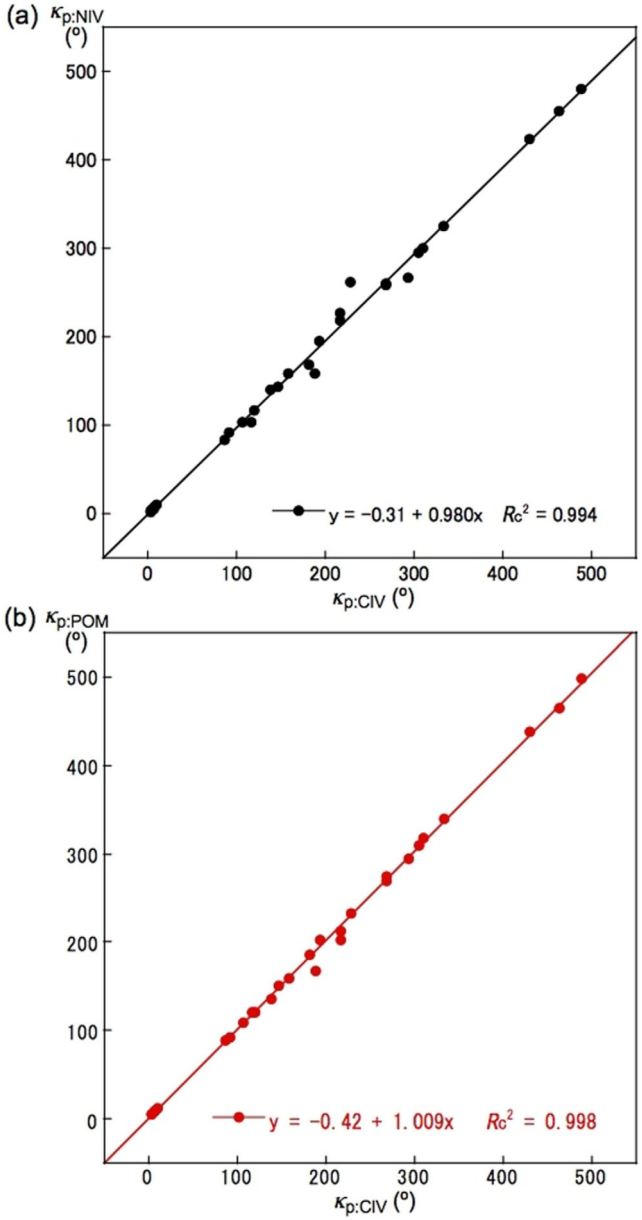

Figure 4. Plots of a) $\kappa_{p:NIV}$ versus $\kappa_{p:CIV}$ and b) $\kappa_{p:POM}$ versus $\kappa_{p:CIV}$.

in the plots. The magnitudes of $\Delta\kappa_{p:NIV-CIV}$ are larger than 10 au^{-1} for H_2S–*–HSH ($\Delta\kappa_{p:NIV-CIV} = 34$ au^{-1}), H_3N–*–HNH_2 (−29 au^{-1}), HBr–*–HBr (−10 au^{-1}), HCl–*–HCl (−27 au^{-1}), H_2O–*–HI (10 au^{-1}), H_2O–*–HBr (−14 au^{-1}), and H_2O–*–HCl (−12 au^{-1}), together with magnitudes of 5 to 10 au^{-1} for HI–*–HI (−8.7 au^{-1}), H_2Se–*–HI (−9.3 au^{-1}), H_2Se–*–HBr (−8.5 au^{-1}), H_2Se–*–HCl (−7.6 au^{-1}), H_2S–*–HI (−9.2 au^{-1}), H_2S–*– HBr (−8.7 au^{-1}), and H_2S–*–HCl (−9.1 au^{-1}). In the case of $\Delta\kappa_{p:POM-CIV}$, the magnitudes are less than 5 au^{-1} for most cases. The values are larger than 10 au^{-1} for H_3N–*–HNH_2 ($\Delta\kappa_{p:POM-CIV} = -37$ au^{-1}), H_2Se–*–HBr (10 au^{-1}), and H_2C=O–*–HI (−14 au^{-1}), together with magnitudes of 5 to 10 au^{-1} for H_2Se–*–HSeH (8.0 au^{-1}), H_2Se–*–HCl (7.1 au^{-1}), H_2S–*–HI (6.2 au^{-1}), and H_2S–*–HBr (8.0 au^{-1}). The magnitudes for $\Delta\kappa_{p:NIV-CIV}$ seem very large at first glance. However, the very large values of κ_p would be responsible for the large magnitudes of $\Delta\kappa_p$ as a whole. The magnitudes of $\Delta\kappa_{p:POM-CIV}$ seem to be much improved relative to the case of $\Delta\kappa_{p:NIV-CIV}$; however, there are some severe deviations, such as H_3N–*–HNH_2 (−37 au^{-1}).

The correlation of $\theta_{p:POM}$ versus $\theta_{p:CIV}$ is much better than that of $\kappa_{p:POM}$ versus $\kappa_{p:CIV}$ (see Table 2, entries 7 and 9). This observation seems curious at first glance, as the same perturbed structures are employed to evaluate θ_p and κ_p in QTAIM-DFA. The differences may be mainly attributable to the much more complex route to evaluate κ_p ($=[d^2y/dx^2]/[1+(dy/dx)^2]^{3/2}$) relative to the case of θ_p ($=90^\circ-\tan^{-1}(dy/dx)$). The θ_p and κ_p values are evaluated by using the common regression curve shown in Equation (7), as pointed out in a previous paper.[49] The small differences in the QTAIM functions based on the perturbed structures generated with CIV and POM will be magni-

fied in the second derivatives of the regression curves used to evaluate κ_p.

As discussed above, the $\theta_{p:POM}$ values can be recognized to be the same as the $\theta_{p:CIV}$ values in terms of the calculation errors as a whole, although the $\Delta\theta_{p:POM-CIV}$ values of -0.7° for H_2O–*–HI and -0.5° for H_2O–*–HBr seem slightly larger than the calculation errors. There must be a reason for these results, but we did not examine this point further. Larger magnitudes of $\Delta\kappa_{p:POM-CIV}$ are usually detected if κ_p is very large. However, the results will not damage the excellent reliability in the characterization of the nHBs, as the κ_p values are not used to characterize the interactions. Namely, the excellent applicability of CIV to generate the perturbed structures for QTAIM-DFA is also well established for the various nHBs, as discussed above.

2.6. Nature of Neutral HBs Evaluated with the (θ, θ_p) Values

The nature of the wide range of HBs for neutral forms **1**–**29** is now classified and characterized on the basis of the θ and $\theta_{p:CIV}$ values obtained in this work. It is instructive to survey the criteria shown in Scheme S2 before a detailed discussion. The θ values classify interactions, whereas the θ_p values predict the character of these interactions. The criteria tell us that $45^\circ < \theta < 180^\circ$ $[0 < H_b(\boldsymbol{r}_c) - V_b(\boldsymbol{r}_c)/2]$ for the CS interactions and $180^\circ < \theta < 206.6^\circ$ $[H_b(\boldsymbol{r}_c) - V_b(\boldsymbol{r}_c)/2 < 0]$ for the SS interactions.[12–16] The CS interactions can be subdivided into $45^\circ < \theta < 90^\circ$ $[H_b(\boldsymbol{r}_c) > 0]$ for the pure CS interactions (*p*-CS) and $90^\circ < \theta < 180^\circ$ $[H_b(\boldsymbol{r}_c) < 0]$ for the regular CS interactions (*r*-CS). In the *p*-CS region of $45^\circ < \theta < 90^\circ$, the character of interactions will be of the vdW type for $45^\circ < \theta_p < 90^\circ$ ($45^\circ < \theta < 75^\circ$), whereas it will be of the typical hydrogen bond (*t*-HB) type with no covalency (*t*-HB_{nc}) for $90^\circ < \theta_p < 125^\circ$ ($75^\circ < \theta < 90^\circ$), for which $\theta = 75^\circ$ and $\theta_p = 125^\circ$ are tentatively given for $\theta_p = 90^\circ$ and $\theta = 90^\circ$, respectively. The CT interaction will appear in the *r*-CS region of $90^\circ < \theta < 180^\circ$. The *t*-HB interactions with covalency (*t*-HB_{wc}) appear in the range of $125^\circ < \theta_p < 150^\circ$ ($90^\circ < \theta < 115^\circ$), for which ($\theta$, θ_p) = (115°, 150°) are tentatively given as the borderline between the *t*-HB_{wc} and CT-MC (interactions in the molecular complex formation through CT) natures. The borderline in the interactions between CT-MC and CT-TBP is defined by (θ, θ_p) = (150, 180°), for which $\theta = 150^\circ$ is tentatively given corresponding to $\theta_p = 180^\circ$. As a result, CT-MC and CT-TBP will appear in the ranges of $150^\circ < \theta_p < 180^\circ$ ($115^\circ < \theta < 150^\circ$) and $180^\circ < \theta_p < 190^\circ$ ($150^\circ < \theta < 180^\circ$), respectively. Namely, the (θ, θ_p) values of (75°, **90**°), (**90**°, 125°), (115°, **150**°), (150°, **180**°), and (**180**°,190°) correspond to the borderlines between the interactions for vdW/*t*-HB_{nc}, *t*-HB_{nc}/*t*-HB_{wc}, *t*-HB_{wc}/CT-MC, CT-MC/CT-TBP, and CT-TBP/Cov-w (weak covalent bonds), respectively. The basic parameters of θ and θ_p, described in bold, are superior to the tentatively given parameters in the classification and characterization of the interactions. The classical chemical bonds of the SS ($180^\circ < \theta$) will be strong if $R > 0.15$ au (Cov-s: strong covalent bonds), whereas they will be weak for $R < 0.15$ au (Cov-w), although SS interactions are not detected in the nHBs studied in this work.

The (θ, $\theta_{p:CIV}$) values of H_2Se–*–HSeH (**1**) are (76.0°, 88.1°), and therefore, it is classified by the *p*-CS interaction and is characterized by its vdW nature (*p*-CS/vdW). The $\theta_{p:CIV}$ value of 88.1° should be superior to $\theta = 76.0^\circ$ ($> 75^\circ$) to predict the nature. The HB interaction in H_3N–*–HNH_2 (**3**) is also predicted to be *p*-CS/vdW in nature with (θ, $\theta_{p:CIV}$) = (74.9°, 87.5°) for the interaction. However, the HB interactions in **1** and **3** would be close to the borderline area between *p*-CS/vdW and *p*-CS/*t*-HB_{nc} judging from the (θ, $\theta_{p:CIV}$) values. HB interactions other than these two were similarly classified and characterized. The nHB interactions are predicted to have the *p*-CS/*t*-HB_{nc} nature for H_2S–*–HSH (**2**), H_2O–*–HOH (**4**), HX–*–HX [**6** (HX = HI), **7** (HBr), and **8** (HCl)], H_2Se–*– HX [**10** (HX = HI), **11** (HBr), and **12** (HCl)], H_2S–*–HI (**14**), and H_2O–*–HI (**18**). The *r*-CS/*t*-HB_{wc} nature is predicted for HF–*–HF (**9**), H_2S–*–HX [**15** (HX = HBr) and **16** (HCl)], H_2O–*–HX [**19** (HX = HBr) and **20** (HCl)], and $H_2C{=}O$–*–HI (**22**). On the other hand, the *r*-CS/CT-MC nature is predicted for H_3N–*–HOH (**5**), H_2Se–*–HF (**13**), H_2S–*–HF (**17**), H_2O–*–HF (**21**), and $H_2C{=}O$–*–HX [**23** (HX = Br), **24** (HCl), and **25** (HF)], whereas the *r*-CS/CT-TBP nature is predicted for H_3N–*–HX [**26** (HX = HI), **27** (HBr), **28** (HCl), and **29** (HF)]. The results are summarized in Table 1. The superior values of θ or θ_p can be employed to predict the nature if either θ or $\theta_{p:CIV}$ does not satisfy the categories to determine the nature. The characterization based on POM is the same as that based on CIV, and the characterization based on NIV is equal to that based on CIV and POM, except for **20** (H_2O–*–HCl). The nature of *r*-CS/CT-MC is predicted for **20** with NIV, whereas it is just borderline between *r*-CS/*t*-HB_{wc} and *r*-CS/CT-MC if evaluated with CIV and POM. The results show that the HB interactions can also be characterized satisfactorily by employing $\theta_{p:NIV}$ for most cases, irrespective of the substantial differences between $\theta_{p:NIV}$ and $\theta_{p:CIV}$ in some cases.

The predicted nature for B–*–HX is summarized in Table 3, exemplified by the formation of B–*–HX from B (= H_2Se, H_2S, H_2O, $H_2C{=}O$, and H_3N) and HX (= HI, HBr, HCl, and HF). It enables us to visualize the roles of B and HX in the formation of B–*–HX. The HB interactions are predicted to be stronger in the order shown in Equations (8) and (9). The results shown in Table 3 and Equations (8) and (9) can be essentially explained on the basis of the results shown in Figure S3, although there are some differences, namely, the order shown in Equation (9) holds for B = H_2Se, H_2S, H_2O, and $H_2C{=}O$ in BH–*–HX, but it is reversed for B = H_3N. The indirect B···(H)–X soft–soft interactions may affect the (θ, $\theta_{p:CIV}$) values in H_2Se–*–HI and H_2S–*–HI.

$$B = H_2Se < H_2S \leq H_2O < H_2C{=}O \ll H_3N \quad (8)$$

$$HX = HI < HBr \leq HCl \ll HF \quad (9)$$

The wide range of nHB interactions in **1**–**29** were satisfactorily classified and characterized by employing the perturbed structures generated with CIV in QTAIM-DFA, resulting in the prediction of the reliable intrinsic dynamic nature of these interactions.

Table 3. The predicted nature of the nHBs in B–*–HX with the (θ, θ_p) values, for which B = H_2Se, H_2S, H_2O, $H_2C{=}O$, and H_3N with HX = HI, HBr, HCl, and HF.[a–c]

HX	B = H_2Se (θ [°], θ_p [°])	nature	H_2S (θ [°], θ_p [°])	nature	H_2O (θ [°], θ_p [°])	nature	$H_2C{=}O$ (θ [°], θ_p [°])	nature	H_3N (θ [°], θ_p [°])	nature
HI	(**88.5**, *126.5*)	*t*-HB_{nc}	(**89.0**, 124.5)	*t*-HB_{nc}	(**84.5**, 113.5)	*t*-HB_{nc}	(95.3, **139.7**)	*t*-HB_{wc}	(164.9, **194.1**)	CT-TBP
HBr	(**87.6**, *130.1*)	*t*-HB_{nc}	(**91.1**, 133.9)	*t*-HB_{wc}	(**93.2**, 138.6)	*t*-HB_{wc}	(*101.6*, **154.6**)	CT-MC	(160.0, **190.3**)	CT-TBP
HCl	(**88.7**, *137.3*)	*t*-HB_{nc}	(**92.8**, 140.5)	*t*-HB_{wc}	(98.9, **149.9**[d])	*t*-HB_{wc}	(*105.9*, **160.4**)	CT-MC	(152.7, **186.9**)	CT-TBP
HF	(*104.3*, **164.5**)	CT-MC	(*108.5*, **165.1**)	CT-MC	(124.0, **166.1**)	CT-MC	(127.8, **170.1**)	CT-MC	(156.4, **182.0**)	CT-TBP

[a] Evaluated with MP2/BSS-A by employing the perturbed structures generated by using CIV. [b] Basic (superior) parameters are shown in bold. In the case of *t*-HB_{wc}, θ is basic if it is close to 90°, whereas θ_p becomes basic if it is close to 150°. [c] Nonsuperior parameters are shown in italics if they do not satisfy the predicted nature on the basis of the superior parameters. [d] The value shows that the nature is borderline between *t*-HB_{wc} and CT-MC.

2.7. Behavior of Neutral HBs, Examined by the Parameters

What is the behavior of the nHBs in **1**–**29**? The behavior was examined on the basis of the relation of ΔE with the compliance force constants (C_{ij}) and the QTAIM (R, θ) and (θ_p, κ_p) parameters for **1**–**29**. Figure 5 draws the plot of ΔE versus C_{ij}. It seems that the plot can be well described by an inverse relationship, although data for $H_3N{\cdots}HX$ [**26** (X = I) and **27** (Br)] deviate from the correlation. Equation (10) shows the inverse relationship for **1**–**29**, except for **26** and **27**. No effort was made to get a best-fit relationship; instead, the averaged value of $\Delta E \times C_{ij}$ (= −165.64) for **1**–**25**, **28**, and **29** was employed in Equation (10). The regression curve, given in Equation (10), is drawn in Figure 5 by a dotted line. The ΔE values for the nHBs seem to be well correlated to C_{ij} if the data for **26** and **27** are omitted. As a result, the stability of B–*–HY, denoted by ΔE, can be well described by the inverse nature of the compliance for the B–*–HY interactions, evaluated by C_{ij}, in **1**–**25**, **28**, and **29**, according to Equation (3).

$$\Delta E \times C_{ij}\ (= xy) = -165.64 \qquad (10)$$

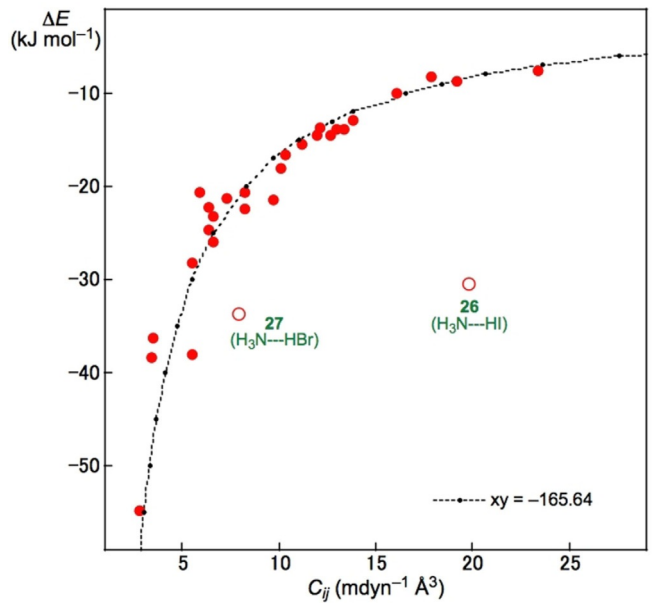

Figure 5. Plot of ΔE versus C_{ij} for **1**–**29**.

The ΔE values for **1**–**29** were next plotted versus R in (R, θ), which is drawn in Figure S4. The correlation is given in Table 2 (entry 10), although the data for **26** and **27** are again omitted from the correlation. The ΔE values in the nHBs of **1**–**25**, **28**, and **29** seem well correlated to R, for which both have the energy unit, although the ΔE values are on the energy surface, whereas the R values are at the BCPs on the BPs corresponding to the HBs. Figure 6 shows the plot of ΔE versus θ for **1**–**29**.

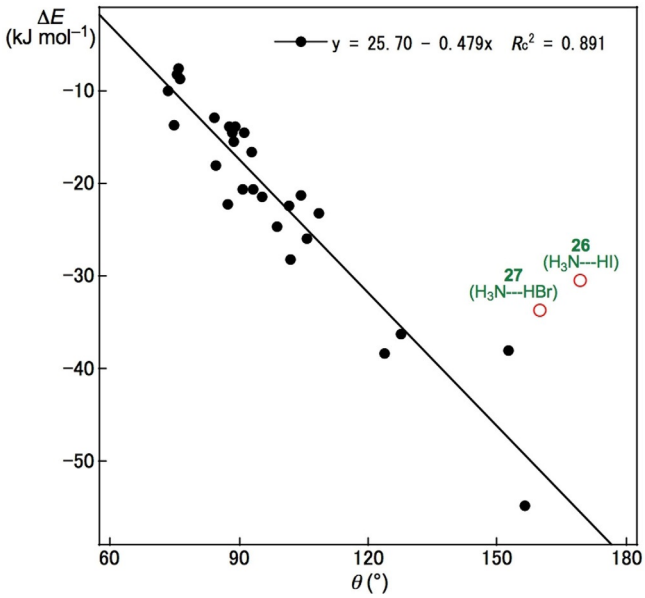

Figure 6. Plot of ΔE versus θ for **1**–**29**.

The correlation seems good if the data of **26** and **27** are omitted from the correlation. The correlation is given in Table 2 (entry 11) (see also Figure 6). Why does ΔE correlate rather well with θ for **1**–**25**, **28**, and **29**? One may not expect such a correlation. However, it is of interest that the plot of θ versus R for **1**–**29** gives a good correlation, although this data is not shown ($\theta = 3956.3R + 64.73$: $R_c^2 = 0.813$). The correlation of ΔE versus R through θ versus R leads to the correlation of ΔE versus θ.

The relations between ΔE and (θ_p, κ_p) are next discussed. Before a detailed discussion is given, the relation between θ_p and θ is examined. The θ_p values are plotted versus θ in Figure S5. A good correlation is obtained for **1**–**20** and **22**–**24**,

which is given in Table 2 (entry 12); the data for **21** (H_2O···HF), **25** (H_2CO···HF), and **26**–**29** (H_3N–HX: X = I, Br, Cl, and F) are omitted from the correlation. Figure 7 illustrates the plot of ΔE versus θ_p for **1**–**29**. The plot was analyzed separately for four groups. Data for **1**–**9** (HA–*–HA) belong to group A [G (A)]. A

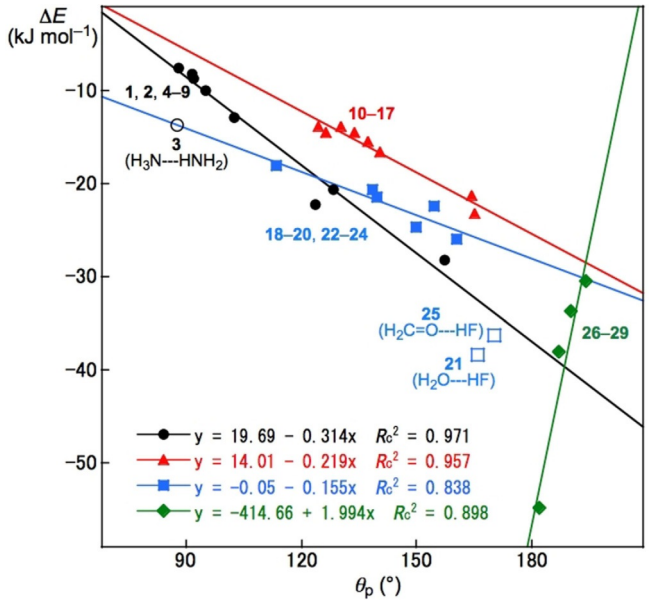

Figure 7. Plot of ΔE versus θ_p for **1**–**29**. Black dots for **1**–**9** belong to G (A), red triangles for **10**–**17** to G (B), blue squares for **18**–**25** to G (C), and green diamonds for **26**–**29** to G (D), although a few deviations are also included.

very good correlation is obtained for G (A), although data for **3** (H_3N–*–HNH_2) deviate from the correlation. The correlation is shown in Table 2 (entry 13). The data for **10**–**17** (H_2Se–*–HX and H_2S–*–HX: X = I, Br, Cl and F) make up group B [G (B)]. Very good correlation is also obtained for G (B), which is shown in Table 2 (entry 14). The data for **18**–**25** (H_2O–*–HX and H_2C=O–*–HX: X = I, Br, Cl, and F) form group C [G (C)]. The correlation seems poorer than those for G (A) and G (B), and the data for **21** (H_2O–*–HF) and **25** (H_2C=O–*–HF) deviate from the correlation. The correlation is given in Table 2 (entry 15). Group D [G (D)] consists of **26**–**29** (H_3N–*–HX: X = I, Br, Cl, and F). A positive correlation constant is predicted for G (D) ($a = 1.99 > 0$; see Table 2, entry 16), contrary to the cases of G (B) and G (C) with negative correlations ($a < 0$; see Table 2, entries 13–15). As shown in Figure 7, ΔE correlates rather well with θ_p as a whole, with a few deviations. The correlation of ΔE versus θ_p should be a reflection of the correlation of ΔE versus θ through the correlation of θ_p versus θ.

The plot of ΔE versus κ_p for **1**–**29** is shown in Figure S6. A linear correlation is not detected between κ_p and ΔE, as expected. The plot shows a characteristic shape. The κ_p values are less than 10 au^{-1} if $\Delta E < -30$ kJ mol^{-1}, 80 $au^{-1} < \kappa_p <$ 300 au^{-1} for -30 kJ $mol^{-1} < \Delta E < -7$ kJ mol^{-1}, and especially 270 $au^{-1} < \kappa_p < 490$ au^{-1} if -17 kJ $mol^{-1} < \Delta E < -10$ kJ mol^{-1}, except for $\kappa_p = 188$ au^{-1} with $\Delta E = -13.8$ kJ mol^{-1} for **6** (HI–*–HI). Very large values of κ_p are observed around the borderline area for HBs between the vdW and *t*-HB_{nc} types.

The stability of the HBs in **1**–**29**, evaluated by ΔE, is well explained on the basis of C_{ij}, R, θ, and θ_p. For the plots of ΔE versus C_{ij}, the magnitudes of ΔE for **26** and **27** seem to be overestimated relative to those expected on the basis of the correlations for **1**–**25**, **28**, and **29**. On the other hand, the magnitudes of ΔE for **26** and **27** would be underestimated relative to those expected from the correlations of ΔE versus R and θ for **1**–**25**, **28**, and **29**. As shown in Figure 7, the plot for ΔE versus θ_p could be recognized as a correlation as a whole, with deviation for G (D) (H_3N–*–HX) from the whole correlation for G (A)–G (C), if the correlation constants for the *a* values for the groups are compared.

3. Conclusions

Hydrogen bonds (HBs) are fundamentally important in all fields of chemical and biological sciences. Therefore, HBs have been variously investigated. However, it has been difficult to characterize the nature of HBs spread over the range of van der Waals (vdW) type for pure closed-shell (CS) interactions to the covalent type of shared-shell (SS) interactions. In this paper, HBs of the neutral form were characterized by applying quantum theory of atoms-in-molecules dual functional analysis (QTAIM-DFA) by employing the perturbed structures generated with CIV. The neutral hydrogen bond (nHB) interactions were characterized on the basis of the static and dynamic behavior predicted with QTAIM-DFA. The static nature arises from the data of the fully optimized structures, whereas the dynamic nature originates from the data of the perturbed structures around the fully optimized structures. The dynamic nature of the interactions could be described as the "intrinsic dynamic nature of interactions" if the perturbed structures were generated with CIV, as the coordinates corresponding to the compliance force constants (C_{ij}), used in CIV, are invariant to the choice of the coordinate system. The method was applied to nHBs and the interactions were characterized. Some of them are as follows: nHBs in H_2Se–*–HSeH and H_3N–*–HNH_2 were characterized by the *p*-CS (pure CS)/vdW nature. The *p*-CS/*t*-HB_{nc} (typical hydrogen bond with no covalency) nature was predicted for H_2S–*–HSH, H_2O–*–HOH, and HX–*–HX (HX = HI, HBr, and HCl), whereas the *r*-CS (regular CS)/*t*-HB_{wc} (*typical*-HB interactions with covalency) nature was predicted for HF–*–HF, H_2S–*–HX (HX = HBr and HCl), and H_2O–*–HX (HX = HBr and HCl). On the other hand, HBs in H_2C=O–*–HX (HX = HBr, HCl, and HF) were predicted to have the *r*-CS/CT-MC (interactions in the molecular complex formation through CT) nature, whereas the *r*-CS/CT-TBP (trigonal bipyramidal adduct formation through CT) nature was predicted for H_3N–*–HX (HX = HI, HBr, HCl, and HF). Characterization based on POM was the same as that based on CIV, and characterization based on NIV was equal to that based on CIV and POM, except for **20** (H_2O–*–HCl). The *r*-CS/CT-MC nature was predicted for **20** with NIV, whereas it was borderline between *r*-CS/*t*-HB_{wc} and *r*-CS/CT-MC if evaluated with CIV and POM. The highly excellent applicability of CIV is well demonstrated in QTAIM-DFA by applying the method to nHBs, in addition to the standard interactions in a previous paper.

Relations between ΔE and C_{ij} or the QTAIM-DFA parameters were examined, together with the reasons. A relation of $\Delta E \times C_{ij} = -165.64$ was found for **1**–**25**, **28**, and **29**. Namely, ΔE could be well described by the inverse nature of C_{ij}. Similarly, the R, θ, and θ_p values correlated linearly well with ΔE. The results showed that the values became larger as the stability of the HBs, described by ΔE, increased in the region examined, although there were a few deviations.

Acknowledgements

This work was partially supported by the Ministry of Education, Culture, Sports, Science and Technology of Japan by a Grant-in-Aid for Scientific Research (No. 17K05785).

Conflict of Interest

The authors declare no conflict of interest.

Keywords: ab initio calculations · atoms-in-molecules dual functional analysis (QTAIM-DFA) · compliance force constants · dynamics · hydrogen bonds

[1] L. Pauling, *The Nature of the Chemical Bond*, Cornell University Press, Ithaca, NY, **1960**.
[2] G. C. Pimentel, A. L. McClellan, *The Hydrogen Bond*, W. H. Freeman, San Francisco, CA, **1960**.
[3] P. Schuster, G. Zundel, C. Sandorfy, *The Hydrogen Bond, Recent Developments in Theory and Experiments*, North-Holland Publishing Company, Amsterdam, **1976**.
[4] G. A. Jeffrey, *An Introduction to Hydrogen Bonding*, Oxford University Press, New York, **1997**.
[5] S. Scheiner, *Hydrogen Bonding, A Theoretical Perspective*, Oxford University Press, Oxford, **1997**.
[6] G. R. Desiraju, T. Steiner, *The Weak Hydrogen Bond in Structural Chemistry and Biology*, International Union of Crystallography Monographs on Crystallography, Oxford University Press, New York, **1999**.
[7] *Hydrogen Bonding: New Insights (Challenges and Advances in Computational Chemistry and Physics)* (Ed.: S. J. Grabowski), Springer, The Netherlands, **2006**, Vol. 3.
[8] "Intramolecular Hydrogen Bonds. Methodologies and Strategies for Their Strength Evaluation": G. Buemi in *Hydrogen Bonding: New Insights (Challenges and Advances in Computational Chemistry and Physics)* (Eds.: S. J. Grabowski), Springer, New York, **2006**, Vol. 3, Ch. 2.
[9] K.-L. Han, G.-J. Zhao, *Hydrogen Bonding and Transfer in the Excited State*, Wiley, Chichester, UK, **2010**.
[10] See the references cited in ref. [41].
[11] W. Nakanishi, S. Hayashi, K. Narahara, *J. Phys. Chem. A* **2008**, *112*, 13593 – 13599.
[12] W. Nakanishi, S. Hayashi, K. Narahara, *J. Phys. Chem. A* **2009**, *113*, 10050 – 10057.
[13] W. Nakanishi, S. Hayashi, *Curr. Org. Chem.* **2010**, *14*, 181 – 197.
[14] W. Nakanishi, S. Hayashi, *J. Phys. Chem. A* **2010**, *114*, 7423 – 7430.
[15] W. Nakanishi, S. Hayashi, *Bull. Chem. Soc. Jpn.* **2012**, *85*, 1293 – 1305.
[16] W. Nakanishi, S. Hayashi, *J. Phys. Chem. A* **2013**, *117*, 1795 – 1803.
[17] S. Hayashi, K. Matsuiwa, M. Kitamoto, W. Nakanishi, *J. Phys. Chem. A* **2013**, *117*, 1804 – 1816.
[18] *Atoms in Molecules: A Quantum Theory* (Ed.: R. F. W. Bader), Oxford University Press, Oxford, **1990**.
[19] "An Introduction to the Quantum Theory of Atoms in Molecules": C. F. Matta, R. J. Boyd in *The Quantum Theory of Atoms in Molecules: From Solid State to DNA and Drug Design* (Eds.: C. F. Matta, R. J. Boyd), Wiley-VCH, Weinheim, Germany, **2007**, Ch. 1.
[20] R. F. W. Bader, T. S. Slee, D. Cremer, E. Kraka, *J. Am. Chem. Soc.* **1983**, *105*, 5061 – 5068.
[21] R. F. W. Bader, *Chem. Rev.* **1991**, *91*, 893 – 926.
[22] R. F. W. Bader, *J. Phys. Chem. A* **1998**, *102*, 7314 – 7323.
[23] R. F. W. Bader, *Acc. Chem. Res.* **1985**, *18*, 9 – 15.
[24] T. H. Tang, R. F. W. Bader, P. MacDougall, *Inorg. Chem.* **1985**, *24*, 2047 – 2053.
[25] F. Biegler-König, R. F. W. Bader, T. H. Tang, *J. Comput. Chem.* **1982**, *3*, 317 – 328.
[26] F. Biegler-König, J. Schönbohm, D. Bayles, *J. Comput. Chem.* **2001**, *22*, 545 – 559.
[27] F. Biegler-König, J. Schönbohm, *J. Comput. Chem.* **2002**, *23*, 1489 – 1494.
[28] J. A. Dobado, H. Martinez-Garcia, J. Molina, M. R. Sundberg, *J. Am. Chem. Soc.* **2000**, *122*, 1144 – 1149.
[29] J. Molina, J. A. Dobado, *Theor. Chem. Acc.* **2001**, *105*, 328 – 337.
[30] S. K. Ignatov, N. H. Rees, B. R. Tyrrell, S. R. Dubberley, A. G. Razuvaev, P. Mountford, G. I. Nikonov, *Chem. Eur. J.* **2004**, *10*, 4991 – 4999.
[31] W. Nakanishi, T. Nakamoto, S. Hayashi, T. Sasamori, N. Tokitoh, *Chem. Eur. J.* **2007**, *13*, 255 – 268.
[32] R. J. Boyd, S. C. Choi, *Chem. Phys. Lett.* **1986**, *129*, 62 – 65.
[33] M. T. Carroll, R. F. W. Bader, *Mol. Phys.* **1988**, *65*, 695 – 722.
[34] S. J. Grabowski, *J. Phys. Chem. A* **2001**, *105*, 10739 – 10746.
[35] E. Espinosa, I. Alkorta, J. Elguero, E. Molins, *J. Chem. Phys.* **2002**, *117*, 5529 – 5542.
[36] I. Rozas, I. Alkorta, J. Elguero, *J. Am. Chem. Soc.* **2000**, *122*, 11154 – 11161.
[37] M. Domagała, S. Grabowski, K. Urbaniak, G. Mloston, *J. Phys. Chem. A* **2003**, *107*, 2730 – 2736.
[38] S. Grabowski, W. A. Sokalski, J. Leszczynski, *J. Phys. Chem. A* **2005**, *109*, 4331 – 4341.
[39] M. Domagala, S. Grabowski, *J. Phys. Chem. A* **2005**, *109*, 5683 – 5688.
[40] Dots are usually employed to show BCPs in molecular graphs. Therefore, A–•–B would be more suitable to describe the BP with a BCP. Nevertheless, A–*–B is employed to emphasize the existence of a BCP on the BP in question in our case.
[41] W. Nakanishi, S. Hayashi, M. B. Pitak, M. B. Hursthouse, S. J. Coles, *J. Phys. Chem. A* **2011**, *115*, 11775 – 11787.
[42] Y. Sugibayashi, S. Hayashi, W. Nakanishi, *Phys. Chem. Chem. Phys.* **2015**, *17*, 28879 – 28891.
[43] S. Hayashi, Y. Sugibayashi, W. Nakanishi, *Phys. Chem. Chem. Phys.* **2016**, *18*, 9948 – 9960.
[44] Y. Sugibayashi, S. Hayashi, W. Nakanishi, *ChemPhysChem* **2016**, *17*, 1804 – 1816.
[45] S. Hayashi, Y. Sugibayashi, W. Nakanishi, *RSC Adv.* **2016**, *6*, 49651 – 49660.
[46] S. Hayashi, Y. Sugibayashi, W. Nakanishi, *RSC Adv.* **2017**, *7*, 31858 – 31865.
[47] S. Hayashi, K. Nagata, S. Otsuki, W. Nakanishi, *J. Phys. Chem. A* **2017**, *121*, 2482 – 2496.
[48] Y. Tsubomoto, S. Hayashi, W. Nakanishi, L. K. Mapp, S. J. Coles, *RSC Adv.* **2018**, *8*, 9651 – 9660.
[49] W. Nakanishi, S. Hayashi, *Int. J. Quantum Chem.* **2018**, *118*, e25590.
[50] K. Brandhorst, J. Grunenberg, *J. Chem. Phys.* **2010**, *132*, 184101 – 184107.
[51] K. Brandhorst, J. Grunenberg, *Chem. Soc. Rev.* **2008**, *37*, 1558 – 1567.
[52] J. Grunenberg, *J. Am. Chem. Soc.* **2004**, *126*, 16310 – 16311.
[53] J. Grunenberg, *Angew. Chem. Int. Ed.* **2001**, *40*, 4027 – 4029; *Angew. Chem.* **2001**, *113*, 4150 – 4153.
[54] J. Böhnke, H. Braunschweig, P. Constantinidis, T. Dellermann, W. C. Ewing, I. Fischer, K. Hammond, F. Hupp, J. Mies, H.-C. Schmitt, A. Vargas, *J. Am. Chem. Soc.* **2015**, *137*, 1766 – 1769.
[55] The C_{ij} values and the coordinates corresponding to C_{ij} were calculated by using the Compliance 3.0.2 program released by Grunenberg and Brandhorst.
[56] Gaussian 09, Revision D.01, M. J. Frisch, G. W. Trucks, H. B. Schlegel, G. E. Scuseria, M. A. Robb, J. R. Cheeseman, G. Scalmani, V. Barone, B. Mennucci, G. A. Petersson, H. Nakatsuji, M. Caricato, X. Li, H. P. Hratchian, A. F. Izmaylov, J. Bloino, G. Zheng, J. L. Sonnenberg, M. Hada, M. Ehara, K. Toyota, R. Fukuda, J. Hasegawa, M. Ishida, T. Nakajima, Y. Honda, O. Kitao, H. Nakai, T. Vreven, J. A. Montgomery, Jr., J. E. Peralta, F. Ogliaro, M. Bearpark, J. J. Heyd, E. Brothers, K. N. Kudin, V. N. Staroverov, R. Kobayashi, J. Normand, K. Raghavachari, A. Rendell, J. C. Burant, S. S. Iyengar, J. Tomasi, M. Cossi, N. Rega, J. M. Millam, M. Klene, J. E. Knox, J. B.

Cross, V. Bakken, C. Adamo, J. Jaramillo, R. Gomperts, R. E. Stratmann, O. Yazyev, A. J. Austin, R. Cammi, C. Pomelli, J. W. Ochterski, R. L. Martin, K. Morokuma, V. G. Zakrzewski, G. A. Voth, P. Salvador, J. J. Dannenberg, S. Dapprich, A. D. Daniels, Ö. Farkas, J. B. Foresman, J. V. Ortiz, J. Cioslowski, D. J. Fox, Gaussian, Inc., Wallingford, CT, **2009**.

[57] T. Noro, M. Sekiya, T. Koga, *Theor. Chem. Acc.* **2012**, *131*, 1124 – 1128.

[58] C. Møller, M. S. Plesset, *Phys. Rev.* **1934**, *46*, 618 – 622.

[59] J. Gauss, *J. Chem. Phys.* **1993**, *99*, 3629 – 3643.

[60] J. Gauss, *Ber. Bunsenges, Phys. Chem.* **1995**, *99*, 1001 – 1008.

[61] F. Biegler-König, *J. Comput. Chem.* **2000**, *21*, 1040 – 1048.

[62] A. Bondi, *J. Phys. Chem.* **1964**, *68*, 441 – 451.

[63] The correlation is $\Delta E = 1.21 + 32.41 \times \Delta r$ ($R_c^2 = 0.876$), if the data for H_3N–*–HF are omitted. The results show that the HB adducts become more stable as the distances are shortened, although H_3N–*–HF is much more stable than that expected from the correlation.

Received: April 5, 2018
Version of record online June 6, 2018

